Depth distribution function calculated by quantum scattering theory

Hiroshi Shinotsuka,* Hiroko Arai, and Takashi Fujikawa
Graduate School of Science, Chiba University, 1-33 Yayoi-cho, Inage-ku, Chiba 263-8522, Japan
(Received 6 October 2007; published 1 February 2008)

The depth distribution function (DDF) $\phi(z)$ in normal photoemission from solids is studied by use of quantum full multiple scattering theory and non-Hermitian optical potential Σ. The damping of the photoelectron waves is taken into account without use of *ad hoc* assumption: Re Σ has influence on the elastic scatterings from surrounding atoms and the Im Σ on the damping of the photoelectron wave. The present theoretical approach explicitly takes the details of atomic arrangement in solids into account, which is in contrast to the currently used classical approaches applied to jellium models. The latter approach cannot study interference effects caused by elastic scatterings from different atomic sites. To properly describe the DDF, full multiple scattering renormalization is inevitable even at 1000 eV, which needs large scale computations. The elastic scatterings give rise to a peak at $z \sim 4.1$ Å in the DDF both for one- and three-dimensional models. Temperature effects on the DDF are also discussed, which smear the DDF because the quantum interference effects are destroyed because of the thermal motions. The asymptotic behavior of $\phi(z)$ for large z shows simple exponential decay from which we can estimate "mean free path." It is, however, different from the original one, since elastic scatterings are renormalized to it.

DOI: 10.1103/PhysRevB.77.085404 PACS number(s): 79.60.−i, 68.35.−p, 78.20.Ci, 78.70.Dm

I. INTRODUCTION

Auger-electron spectroscopy and x-ray photoelectron spectroscopy (XPS) have developed rapidly, which are now used extensively in many different areas of science and technology. Excited electrons from solids travel some distance before they escape through the solid surface. During this transport, some electrons lose energy through inelastic scatterings. This gives rise to an attenuation of the peak intensity as well as to a background signal of inelastic electrons.[1] For any quantitative analyses of these spectra, we need procedures to correct for these spectral changes influenced by elastic scatterings. The main approach to account for elastic scatterings was the Monte Carlo method.[2–5] However, the statistical uncertainty associated with the Monte Carlo simulations gives rise to very long computation times. Hence, analytical and semianalytical methods have been proposed.[6–8] One of the prospective methods for deriving the analytical expressions is approximate solutions of the Boltzmann equation. In these classical approaches, they take into account inelastic collisions with the electrons in the target as well as elastic collisions with the randomly distributed ionic cores.[8] It is, thus, impossible for us to discuss the geometrical effects on these spectroscopies.

To describe the attenuation, the inelastic mean free path (IMFP) and the depth distribution function (DDF) are key factors. The DDF is defined as "the probability that the electrons leaving the surface in a specified state originated from a specified depth measured normally from the surface."[9] In several theoretical and experimental studies, they have found that the DDF of photoelectrons from *s* subshells leaving a surface in certain directions exhibits complex behavior, with a maximum at the depth comparable to the IMFP. For example, Tilinin *et al.* have obtained a peak in DDF at the normal photoemission excited from O 1*s* level in Al_2O_3 grown on Al substrate. In contrast to this complicated behavior, the DDF recorded at the polar emission angle $\alpha=60°$ shows a simple exponential decay as a function of the depth.[10] Quite similar results are obtained for O 1*s* photoelectrons from copper oxide[11] and iron oxide,[12] and for S 2*s* photoelectrons from silver sulphide.[13]

Although the above theoretical tools have successfully been used for the analyses of the DDF, they completely neglect the quantum interference associated with electron elastic scatterings from composite atoms. It is, thus, important for us to apply purely quantum approaches to the DDF calculations in order to study the applicability of the widely used classical methods. Of course, quantum calculations must be much harder than the classical ones.

In order to take the damping of the photoelectron waves from first principles, two different theoretical approaches have been used. Simple but very useful practical many-body scattering approach has been developed by Hedin and coworkers using the projection operator technique.[14,15] The second approach, Keldysh Green's function theory, is more formal than the above approaches.[16–18] Skeleton diagram expansion in terms of dressed one-electron Green's functions and the screened Coulomb interaction yields useful formulas to study resonant effects including multiatom resonant effects[19] and losses (intrinsic+extrinsic).[20,21] Both of the first principle theories successfully explain the reason why these electron spectroscopies are surface sensitive by use of the damping photoelectron wave function under the influence of non-Hermitian energy dependent optical potential Σ. Of course, the details of Σ are different for the different approaches. The former can easily take the hole effects into account, whereas the latter the temperature effects and so on.

In this paper, we calculate the DDF based on the many-body quantum mechanical multiple scattering theory developed by us to study photoelectron diffraction spectra,[22–25] where the optical potential is explicitly calculated. So far, no quantum theoretical approach has been applied to study DDF. We, thus, have had no detailed information on the importance of the interference effects associated with the quan-

tum elastic scatterings which reflects the details of local atomic arrangements around an x-ray absorbing atom.[25] In this theoretical framework, IMFP is introduced in a slightly different way from the usual IMFP which can be calculated for electron gas models,[26] where atomic potentials are completely neglected (see Sec. III B). The present theoretical framework, however, explicitly includes elastic scatterings from each atomic site and damping effects. The IMFP for jellium should be different from that for real solids. We, however, find that the difference is quite small. In this work, we only consider the normal emission because of very long computation time, so that off-normal emission has not been discussed.

II. THEORY

A. General multiple scattering photoemission formula

First principle many-body photoemission theories give us a useful formula for x-ray photoelectron diffraction (XPD) amplitude $M(\boldsymbol{k})$ measuring photoelectron momentum $\boldsymbol{k}$, which is written by

$$M(\boldsymbol{k}) = \langle \psi_{\boldsymbol{k}}^{-} | \Delta | \phi_c \rangle S_0 + \cdots, \tag{1}$$

where $\psi_{\boldsymbol{k}}^{-}$ is the photoelectron wave function under the influence of optical potential Σ in a system, Δ the electron-photon interaction operator, and ϕ_c a wave function of a core orbital localized on the site A. The site A also means x-ray absorbed atom and the photoelectron emitter. The intrinsic amplitude S_0 describes the reduction associated with the core-hole production, which is written in terms of the initial target state $|0\rangle$, no-loss hole state $|0^*\rangle$, and the annihilation operator b for the core state ϕ_c,

$$S_0 = \langle 0^* | b | 0 \rangle.$$

In principle, the amplitude S_0 depends on the depth of the photoelectron emitter A.[15] However, the depth dependence is supposed to be weak enough,[15] so that we neglect it from now on. In comparison with the no-loss bands, prominent loss bands, for example, plasmon loss peaks, cannot be described by Eq. (1) (Refs. 14, 15, and 20): In this case, the quantum interference should explicitly be taken into account.

By use of the site-t matrix expansion of $\psi_{\boldsymbol{k}}^{-}$,[22–25] the amplitude neglecting the factor S_0 can be written by the multiple scattering series,

$$M(\boldsymbol{k}) = Z_1 + Z_2 + Z_3 + \cdots, \tag{2}$$

where Z_1 is the amplitude without scatterings from surrounding atoms (direct term), Z_2 is the single-scattering amplitude, Z_3 is the double-scattering amplitude, and so on. The direct term Z_1 is explicitly written by

$$Z_1 = \langle \phi_{A\boldsymbol{k}}^{-} | \Delta | \phi_c \rangle = \sum_L Y_L(\hat{\boldsymbol{k}}) M_{LL_c}, \tag{3}$$

where $\phi_{A\boldsymbol{k}}^{-}$ is the photoelectron wave function emitted from an x-ray absorbed atom A, and L is the abbreviated form of the pair of angular momentum, $L=(l,m)$. In the dipole approximation, the photoexcitation matrix element M_{LL_c} excited by linearly polarized light parallel to the z axis is given by

$$M_{LL_c} = \sqrt{\frac{2}{\pi}} i^{-l} e^{i\delta_l^A} \rho(l)_c G(L_c 10|L), \tag{4}$$

$$\rho(l)_c = \int R_l(kr) R_{l_c}(r) r^3 dr, \tag{5}$$

where δ_l^A is the phase shift of lth partial wave at site A, and $R_l(kr)$ and $R_{l_c}(r)$ describe the radial part labeled by the orbital angular momentum of $\phi_{A\boldsymbol{k}}^{-}$ and ϕ_c, respectively. Gaunt integral $G(L_c 10|L) = \int Y_{L_c}(\boldsymbol{r}) Y_{10}(\boldsymbol{r}) Y_L^*(\boldsymbol{r}) d\hat{\boldsymbol{r}}$ is responsible for the angular momentum selection rule of the photoexcitation. The single-scattering term Z_2 is explicitly written by

$$\begin{aligned} Z_2 &= \sum_{\alpha(\neq A)} \langle \phi_{\boldsymbol{k}}^0 | t_\alpha g_A \Delta | \phi_c \rangle \\ &= \sum_{\alpha(\neq A)} e^{-i\boldsymbol{k}\cdot\boldsymbol{R}_{\alpha A}} \sum_{LL'} Y_{L'}(\hat{\boldsymbol{k}}) t_{l'}^{\alpha}(k) G_{L'L}(k\boldsymbol{R}_{\alpha A}) M_{LL_c}, \end{aligned}$$

$$g_A = g_0 + g_0 t_A g_0, \tag{6}$$

where $\phi_{\boldsymbol{k}}^0$ is the plane wave and $\boldsymbol{R}_{\alpha A}$ is the position vector of scatterer α measured from a photoelectron emitter A. The angular momentum representation of the site-t matrix $t_l^{\alpha}(k)$ at site α is given by

$$t_l^{\alpha}(k) = -\frac{e^{2i\delta_l^{\alpha}} - 1}{2ik} \tag{7}$$

in terms of the phase shift δ_l^{α} at site α and the photoelectron wave number k. The propagator $G_{L'L}(k\boldsymbol{R}_{\alpha A})$ describes electron propagation from the site A with L to the site α with L'.[27] In terms of $X=tG$, we obtain the general renormalized multiple scattering XPD formula,[22]

$$\begin{aligned} M(\boldsymbol{k}) &= \sum_{\alpha} e^{-i\boldsymbol{k}\cdot\boldsymbol{R}_{\alpha A}} \sum_{LL'} Y_{L'}(\hat{\boldsymbol{k}}) [1 + X + X^2 + X^3 + \cdots]_{L'L}^{\alpha A} M_{LL_c} \\ &= \sum_{\alpha} e^{-i\boldsymbol{k}\cdot\boldsymbol{R}_{\alpha A}} \sum_{LL'} Y_{L'}(\hat{\boldsymbol{k}}) [(1-X)^{-1}]_{L'L}^{\alpha A} M_{LL_c}, \end{aligned} \tag{8}$$

$$X_{LL'}^{\alpha\beta} = t_l^{\alpha}(k) G_{LL'}(k\boldsymbol{R}_{\alpha\beta})(1 - \delta^{\alpha\beta}), \tag{9}$$

where X is a square matrix, in which a matrix element is labeled by a set of atomic sites (A, $\alpha,\beta,\ldots$) and angular momentum L, whose matrix dimension is $N(l_{\max}+1)^2$ for the cluster of N atoms and maximum angular momentum $l_{\max}$. The full multiple scattering is taken into account by use of the inverse matrix $(1-X)^{-1}$.

B. Electron attenuation

In this section, we study the effects of an electron attenuation in the above XPD theory. For that purpose, several optical potential theories have been developed.[28–32] Equation (1) is derived from first principle many-body theory without additional *ad hoc* assumption.[14] The nonlocal optical potential $\Sigma(\varepsilon_k)$ has now Hermitian (real) and anti-Hermitian (imaginary) parts

$$\Sigma(\varepsilon_k) = V - i\Gamma. \tag{10}$$

The real part V substantially influences the phase shifts, and the imaginary part $-i\Gamma$ is responsible for the photoelectron damping, which typically weakly depends on the space, and is approximated by a constant. To apply the site-t matrix expansion, we have two different choices of the free propagator g_0.

At first we define the damping free propagator $g_0(\varepsilon)$,

$$g_0(\varepsilon) = \frac{1}{\varepsilon - T_e + i\Gamma_0} \quad (\Gamma_0 > 0), \tag{11}$$

where T_e is the kinetic energy operator, $T_e = p^2/2$. This choice definitely makes $\phi_{\boldsymbol{k}}^0$ in Eq. (6) the damping plane wave, with the complex momentum $\boldsymbol{k}'$ defined by Eq. (12). When Γ_0 is determined as a muffin-tin constant and the residual imaginary part is small in each muffin-tin sphere, the phase shifts δ_l^α are completely influenced by $V_H + V$, where V_H is the Hartree potential. We can write the total potential $V_H + V$ as the sum of each atomic potential v_α,

$$V_H + V = \sum_\alpha v_\alpha.$$

By use of this separation, we can apply the site-t matrix expansion[22–25]

$$g(\varepsilon) = g_0(\varepsilon) + \sum_\alpha g_0(\varepsilon) v_\alpha g_0(\varepsilon) + \cdots$$

$$= g_A(\varepsilon) + \sum_\alpha g_0(\varepsilon) t_\alpha g_A(\varepsilon) + \cdots.$$

We can also use another expansion in terms of a free propagator without damping instead of the above damping free propagator

$$g_0(\varepsilon) = \frac{1}{\varepsilon - T_e + i\eta} \quad (\eta \to +0).$$

In such a case, $\phi_{\boldsymbol{k}}^0$ in Eq. (6) should be pure plane wave, and we have to divide $V_H + \Sigma$ into each atomic potential v'_α. In this case, the potential $V_H + \Sigma$ in the interstitial region is finite, which can give rise to redundant scatterings. The atomic scattering phase shifts δ_l^α should be complex.

The former expansion naturally describes the photoelectron wave propagation with damping, and we use this expansion hereafter. The effective momentum $\boldsymbol{k}'$ is, thus, defined by the principal value

$$k' = \sqrt{2(\varepsilon_k + i\Gamma_0)} \equiv k_r + i\kappa \quad (\boldsymbol{k}' \parallel \boldsymbol{k}). \tag{12}$$

In the high energy region ($\varepsilon_k \gg \Gamma_0$), κ is approximated by

$$\kappa = \frac{\Gamma_0}{k} \sim -\frac{1}{k} \operatorname{Im} \Sigma.$$

This expression gives the widely used IMFP formula.[33] We should, however, notice that there exists an important difference between them. In the present approach, Γ_0 is determined so as to get rid of redundant scatterings from the interstitial region. In the atomic regions atomic potential including the real part of Σ is fully taken into account. In the conventional approaches, Γ_0 is determined for jellium model neglecting atomic potentials.

In this work, we use the Hedin-Lundqvist potential for the optical potential calculations.[34,35] More sophisticated approaches have been developed now,[30] but additional average is to be devised to obtain Γ_0.

We, thus, have the photoemission amplitude explicitly including the damping effects,

$$M(\boldsymbol{k}) = \sum_\alpha e^{-\kappa D_\alpha(\hat{\boldsymbol{k}})} e^{-i\boldsymbol{k}_r \cdot \boldsymbol{R}_{\alpha A}} \sum_{LL'} Y_{L'}(\hat{\boldsymbol{k}}) [(1-X)^{-1}]^{\alpha A}_{L'L} M_{LL_c}, \tag{13}$$

$$X^{\alpha\beta}_{LL'} = t_l^\alpha(k_r) G_{LL'}(k_r \boldsymbol{R}_{\alpha\beta}) e^{-\kappa \boldsymbol{R}_{\alpha\beta}} (1 - \delta^{\alpha\beta}). \tag{14}$$

where $D_\alpha(\hat{\boldsymbol{k}})$ is the distance from the site α to the surface of the solid along the direction of a photoelectron propagation $\hat{\boldsymbol{k}}$.

C. Debye-Waller factor

For practical purposes, we introduce Debye-Waller factors to take account of thermal and static disorder on photoemission intensities. First, we should calculate the photoemission intensity at a fixed nuclear arrangement and, next, take the thermal average of it over all possible nuclear fluctuations around an equilibrium configuration,[36,37] so that the coherent sum renormalization as used to derive $(1-X)^{-1}$ is not allowed. To derive the coherent sum, we assume the random phase cancellation for cross products of complicated multiple scattering terms, which yields

$$M(\boldsymbol{k}) \sim \sum_\alpha e^{-\kappa D_\alpha(\hat{\boldsymbol{k}})} e^{-i\boldsymbol{k}_r \cdot \boldsymbol{R}_{\alpha A}} \sum_{LL'} Y_{L'}(\hat{\boldsymbol{k}}) [(1 - X(T))^{-1}]^{\alpha A}_{L'L} M_{LL_c}, \tag{15}$$

where the matrix $X(T)$ is temperature dependent through the Debye-Waller factor $\sigma^2_{\alpha\beta}$,

$$X^{\alpha\beta}(T) = X^{\alpha\beta} \exp(-k^2 \sigma^2_{\alpha\beta}). \tag{16}$$

In the above derivation, we have used the harmonic approximation for the lattice vibration.[38]

To calculate the Debye-Waller factor, we use the Debye approximation, which gives

$$\sigma^2_{\alpha\beta} = \frac{\hbar}{M} \int_0^{\omega_D} d\omega \frac{3\omega}{\omega_D^3} \left\{ 1 - \frac{\sin(R_{\alpha\beta}\omega/c)}{R_{\alpha\beta}\omega/c} \right\} \coth(\beta\hbar\omega/2), \tag{17}$$

where $\beta = (k_B T)^{-1}$, M is the reduced mass of atoms α and β, ω_D is the Debye frequency, related to Debye temperature Θ_D by $k_B \Theta_D = \hbar\omega_D$, and c is sonic velocity in the solid; they are related by $\omega_D^3 = 6n\pi^2 c^3$, where n is a density of lattice points. The Debye approximation works well for the monatomic crystals considered here; however, optical modes approximated by Einstein models are also to be taken into account for complex solids except for the monatomic solids.[36,39] We, thus, have the photoemission intensity excited from the core

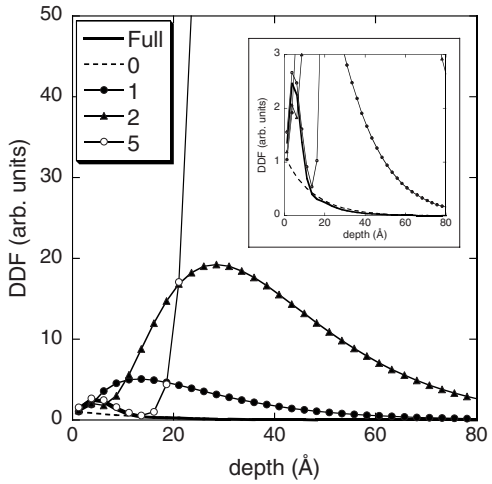

FIG. 1. The effects of the scattering orders on the DDFs excited from Fe 2*s* level for the chain model (Fe_{50}, chain length=123 Å); ε_k=1000 eV and l_{max}=17. "0" stands for the photoemission intensity $|Z_1|^2$, "1" for $|Z_1+Z_2|^2$,…, and "Full" for $|Z_1+Z_2+\cdots|^2$. The inset shows the expanded DDF.

level c on site A neglecting unimportant constants

$$I_A \sim \left| \sum_{\alpha} e^{-\kappa D_{\alpha}(\hat{\mathbf{k}})} e^{-i\mathbf{k}_r \cdot \mathbf{R}_{\alpha A}} \sum_{LL'} Y_{L'}(\hat{\mathbf{k}}) [[1 - X(T)]^{-1}]^{\alpha A}_{L'L} M_{LL_c} \right|^2. \tag{18}$$

This equation directly gives the DDF $\phi(z_A)$.

III. CALCULATED RESULTS

In this section, we show some calculated DDFs for iron crystals by use of the full multiple scattering approaches described in the previous section. We use two different models for the clusters to analyze the DDF. One is a simplified model; one-dimensional model where only forward and backward scatterings are considered. Another model is more realistic: three-dimensional one where elastic scatterings from all atoms in cylinders are taken into account. Of course, computation cost is much smaller for the one-dimensional model than that for the latter.

A. One-dimensional Fe chain

We first study the DDF in normal photoemission from the one-dimensional Fe chains along the z axis, where the matrix elements $X_{LL'}$ vanish when $m=0$ or $m'=0$. We consider the excitation from the Fe 2*s* level irradiated by linearly polarized x rays parallel to the z axis. The chain length is 123 Å, composed of 50 Fe atoms whose interatomic distance is 2.48 Å, referring to that in bcc iron crystals. Iron (001) surface has two different types of chains as shown by C_1 and C_2 in the inset of Fig. 6. Here, we simplify the model where all atoms are in the same chain, with the distance in iron crystals. We neglect the Debye-Waller factors here.

Figure 1 shows the calculated DDFs with ε_k=1000 eV for different multiple scattering orders: "0" stands for the direct photoemission intensity $|Z_1|^2$, "1" $|Z_1+Z_2|^2$,…, and "Full" for $|Z_1+Z_2+\cdots|^2$, where the full multiple scatterings are taken into account. Here, we neglect the Debye-Waller factors. To calculate the DDF, we should include partial waves up to l_{max}=17 for the kinetic energy ε_k=1000 eV after we check the convergence. The inset shows the expanded DDF to distinguish "Full" and "0." The DDF "0" without scattering effects from surrounding atoms shows simple exponential decay as expected. This result corresponds to the so-called straight line approximation.[2] The calculated results for the single-scattering approximation $|Z_1+Z_2|^2$ shows a peak at ~15 Å depth, and the double-scattering approximation $|Z_1+Z_2+Z_3|^2$ gives a peak at ~30 Å, and the DDF diverges with scattering orders. The peak in DDF is typically observed at the depth comparable to the IMFP.[10–13] On the other hand, the full multiple scatterings give reasonable result for the peak position. This result is quite different from that observed in XPD analyses. At the high energy region considered here (1000 eV), XPD patterns usually converge with a few forward multiple scatterings.[25,40] In XPD studies, small take-off angle detection (<10°) is usually used to obtain surface sensitive spectra. We, hence, use only full multiple scatterings from now on.

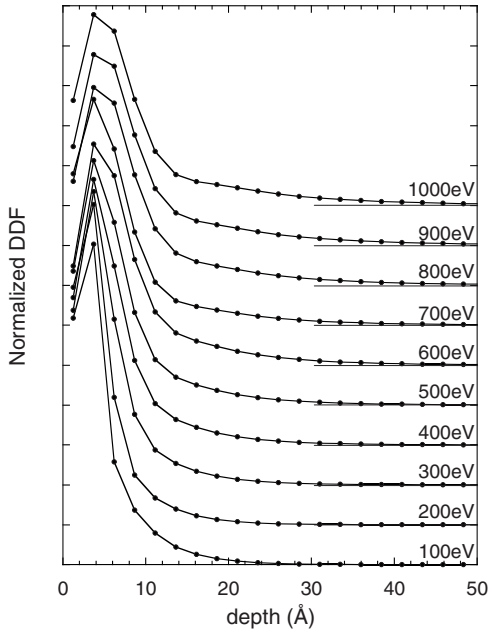

FIG. 2. Fe 2*s* DDF for different ε_k from 100 to 1000 eV. The horizontal lines on the right side show the baselines of the DDF for each energy.

Next, we examine the energy dependence of DDFs. Figure 2 shows the DDF from Fe 2*s* photoemission for different photoelectron energies ε_k=100–1000 eV for the same chain models used in Fig. 1. We normalize the DDF $\phi(z)$ so as to be

$$\int_0^{\infty} \phi(z) dz = 1$$

to closely compare the depth profile where z is the depth of the emitter from the surface. Filled circles show the iron

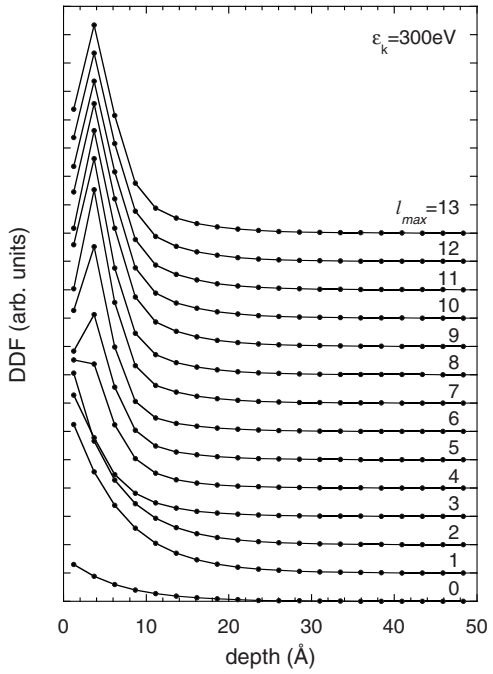

FIG. 3. DDF for different $l_{\max}$ with $\varepsilon_k=300$ eV.

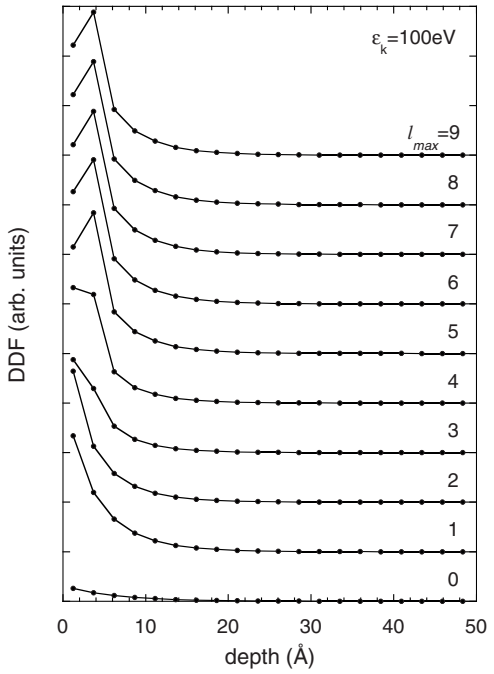

FIG. 4. Same as Fig. 3, but with $\varepsilon_k=100$ eV.

lattice sites from which photoelectrons are ejected. A prominent sharp peak at ~5 Å is observed for all calculated energies ($\varepsilon_k \geqslant 100$ eV). With increase of ε_k, the peak broadens but does not shift. For high energy photoemission, the contribution from deep sites is important because of the large IMFP: The breakdown of the exponential decay should be caused by the focusing effects as widely observed in XPD[25] and in extended x-ray-absorption fine structure (EXAFS) spectra.[41]

We next investigate $l_{\max}$ dependence of the calculated DDF. Figure 3 shows the $l_{\max}$ dependence for Fe 2*s* photoemission intensity with $\varepsilon_k=300$ eV for the same models used in Fig. 1. For $l_{\max}=0-4$, no peak is observed in the DDF, whereas a peak is observed when $l_{\max} \geqslant 5$. This result is also related to the focusing effects: We expect the strong focusing effects for large $l_{\max}$. We find a good convergence for $l_{\max}=10$; larger $l_{\max}$ gives no prominent difference in the DDF. We also study the $l_{\max}$ dependence for lower photoemission energy $\varepsilon_k=100$ eV. As shown in Fig. 4, the DDF at $\varepsilon_k=100$ converges for smaller $l_{\max}$, $l_{\max}=5$, because $l_{\max}$ is approximately written by $l_{\max}=ka$ within one-electron potential scattering theory, where a is the impact parameter. In our treatment, we use a more sophisticated approach without the use of such a simple model, so that $l_{\max}$ is not proportional to k. Let us consider the reason why we can observe a peak in the DDF when $\varepsilon_k \geqslant 100$ eV fixed at $l_{\max}=17$ in Fig. 2, and when $l_{\max} \geqslant 5$ fixed at $\varepsilon_k=300$ eV in Fig. 3. The focusing effects are important for large ε_k, where large $l_{\max}$ should inevitably be used. The photoemission intensity from an atom in the second layer is smaller than that from an outermost atom with the damping factor $e^{-2\kappa d}$ (d is the distance from the surface) when we neglect the forward scatterings from the surface atom. On the other hand, the forward scattering gives an enhanced factor in the order of $|f_\alpha(0)|^2$, where $f_\alpha(0)$ is the forward scattering amplitude. Strong focusing effects (large $|f_\alpha(0)|^2$) can give the larger photoemission intensity from the second layer than that from the first layer. For the photoemission from the deeper sites, the exponential damping plays a more important role than the forward elastic scatterings.

Figure 5 shows the calculated DDF for different chain lengths from short (5 atoms, 11 Å) to longer chains (50 atoms, 123 Å) with $\varepsilon_k=300$ eV: We neglect the Debye-Waller factors. We only observe the very small difference between them: The chain length is not so important for the DDF calculations because the forward scatterings are dominant. Of

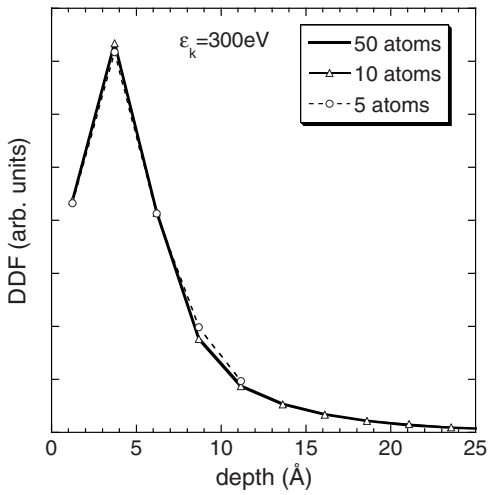

FIG. 5. Calculated DDFs for different chain lengths with $\varepsilon_k=300$ eV. The lengths of the chains are 11 Å (5 atoms), 24 Å (10 atoms), and 123 Å (50 atoms).

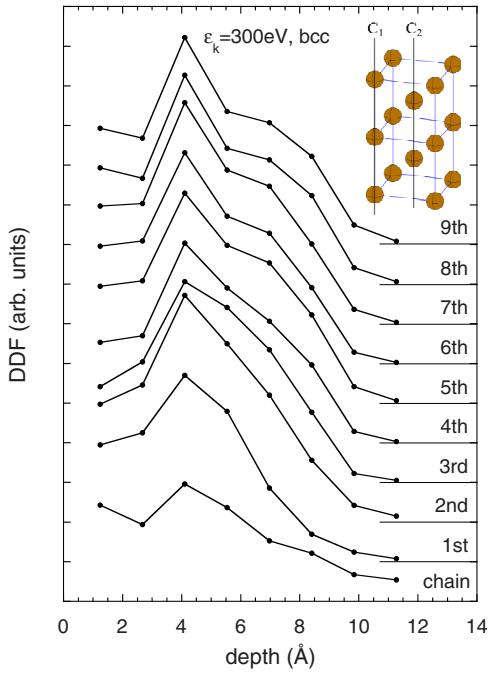

FIG. 6. (Color online) Calculated DDFs from Fe (001) surface where we use cylindrical bcc models with different radii for ε_k =300 eV. The horizontal lines on the right side describe the baselines of the DDF $\phi(z)$ for each size. In the inset, two different types of chains C_1 and C_2 are shown.

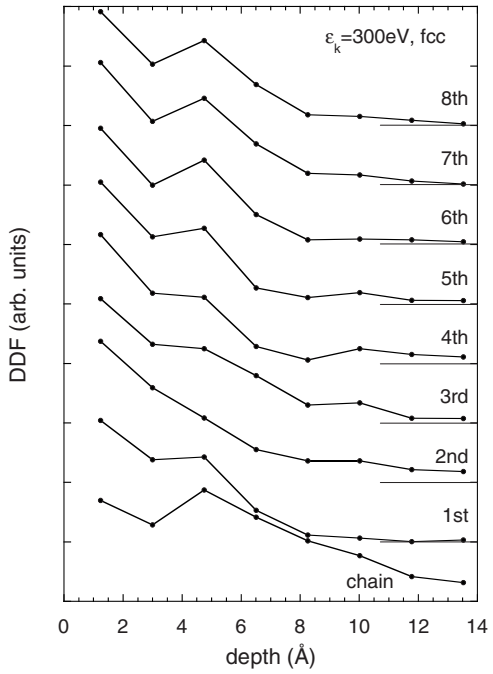

FIG. 7. Same as Fig. 6, but artificial fcc cylinder models are used here.

course, the chain length should be slightly larger than the depth at which the DDF $\phi(z)$ is to be calculated.

B. Three-dimensional Fe model

In this section, we use more realistic models than the chain models considered before, where we only consider the forward and backward scatterings in the chain. In addition to them, we also consider elastic scatterings with small angles; surrounding atoms around the z axis in a finite size cylinder are taken into account. All multiple scatterings inside these cylindrical clusters are fully taken into account. We consider the photoemission from Fe (001) surface, neglecting the Debye-Waller factors: The two chains C_1 and C_2 in the inset of Fig. 6 have different distributions of Fe atoms measured from the surface. In the chain C_1, there exists an outermost surface atom, whereas in the chain C_2, an atom in second layer occupies the top site. We, thus, use the two different cylinders whose central chains are C_1 and C_2. We change the cylinder radius up to the ninth sheet (up to the radius 8.1 Å) around the emitter atoms. The calculated results for these models are shown in Fig. 6. The intensity from the third layer in the cylinder models is much larger than that from the chain model with the same length. When the radius becomes larger, the DDF converges at the eighth sheet. In the one-dimensional chain model, the peak is not so sharp and the DDF slowly decays with z in comparison with the cylinder models. The peak is observed at the third layer, whereas the depth is nearly the same (~4 Å) for the chain and the cylinder models. This result clearly shows that the chain models successfully predict a peak in DDF due to focusing elastic scatterings, whereas they are poor in describing the decay profile of the DDF, in particular, at $z>10$ Å as discussed below.

We next study the sensitivity of the DDF to the details of the atomic arrangements. For that purpose, we consider an artificial "fcc" iron lattice including eight layers (13.5 Å). The DDF from fcc Fe (001) surface is shown in Fig. 7, where the result for the chain model is also shown for comparison. To keep the Fe-Fe distance the same as before, we use the lattice constant 3.51 Å for this artificial crystal. The calculated DDF features are quite different from the previous ones: The peak observed at the third layer (~4.1 Å) is less sharp than that in the bcc model. We can explain this result based on XPD theory, where the detailed atomic arrangements influence the XPD pattern:[22–25] For small z, the XPD effects are dominant.

C. Temperature dependence of the depth distribution function

We next study the temperature dependence of the DDF for the Fe chain models considered in Sec. III A, and for the cylinder models in Sec. III B. We should note that the chain model is a cluster, inside which full multiple scatterings are taken into account. The phonon modes are calculated on the basis of three-dimensional crystals, where we have a simple relation $\omega=ck$ in the Debye model. For the present studies, we calculate the Debye-Waller factors by use of Eq. (17) in the Debye approximation, where we use Θ_D=467 K for iron crystals. For example, $\sigma^2_{\alpha\beta}=0.260\times10^{-2}$ Å^2 at 0 K, and 0.537×10^{-2} Å^2 at 300 K for interatomic distance $R_{\alpha\beta}$ =2.867 Å. Figure 8 shows the result for the chain models Fe_{50} used before for different temperatures from 0 to 700 K.

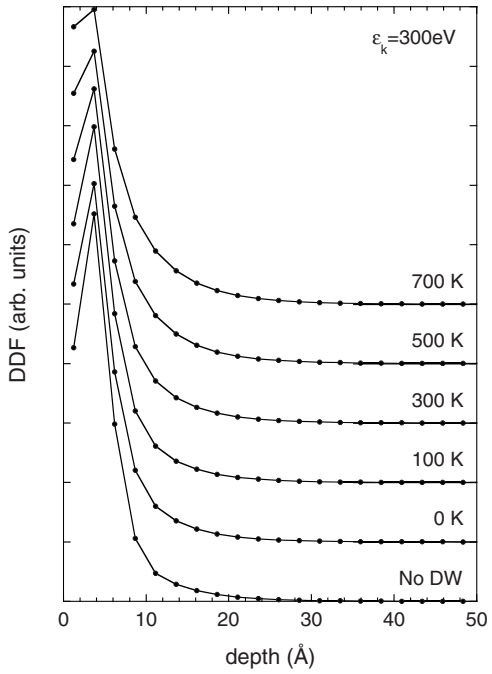

FIG. 8. Temperature dependent DDF from the chain model Fe_{50} used in Figs. 1–4 with $\varepsilon_k=300$ eV. The Debye-Waller factor is calculated in the Debye approximation [see Eq. (17)]. For comparison, the result with no Debye-Waller factor is also shown (No DW).

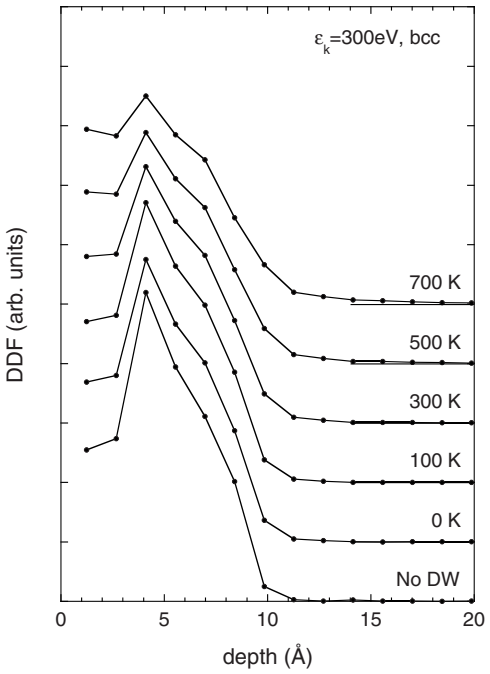

FIG. 9. Same as Fig. 8, but from the bcc cylinder model, Fe_{198}.

Even at 0 K, zero-point oscillation makes a difference from the result where the Debye-Waller factor is completely neglected. For lower temperature, the peak is sharp, which reflects the importance of elastic scatterings to give the prominent peak: The Debye-Waller factor destroys the interference. Figure 9 also shows the temperature dependence of the DDF for the Fe cylinder models including 198 atoms in the cylinder, $h=25.9$ Å, and $r=4.6$ Å. We observe a temperature dependence similar to those in Fig. 8. We should note that the decay profile at large z is also influenced by the temperature: At higher temperature, the DDF decays slowly both in the chain and in the cylinder models, which imply the importance of the elastic scatterings for the DDF even at deep depth. The details are discussed below.

D. Depth distribution function at large z

The asymptotic behavior of $\phi(z)$ at large z is well described by a simple exponential law

$$\phi(z) \sim \phi_0 e^{-z/\lambda_d}, \tag{19}$$

where λ_d is the dressed IMFP, which effectively includes the elastic scattering effects. Of course, this law does not work at small z as seen in the previous sections. Figure 10 shows $\ln \phi(z)$ as function of the depth z for different photoelectron energies, $\varepsilon_k=100$, 300, 500, and 1000 eV, where we use the chain model used in Fig. 1 and neglect the Debye-Waller factors again. For comparison, $\ln \exp(-z/\lambda)$ are also plotted, where the bare IMFP λ is calculated by $\lambda=(2\kappa)^{-1}$. All of them are well fitted to linear straight lines in the large z region (>80 Å). In the low energy case ($\varepsilon_k=100$ eV), the linear fitting is good even in the region $z>30$ Å. On the other hand, it is good only in the region $z>80$ Å for the higher energy case ($\varepsilon_k=1000$ eV). The IMFP is short for the low energy photoemission, and the exponential decay starts even at small z. This figure clearly shows that the approximation (19) works well for large z, but λ_d is not simply λ, because elastic scatterings are renormalized in the exponential decay formula. The linear fitting provides λ_d for different energies, which are listed in Table I. Tanuma *et al.* have used Penn's algorithm to calculate IMFP in a wide range of

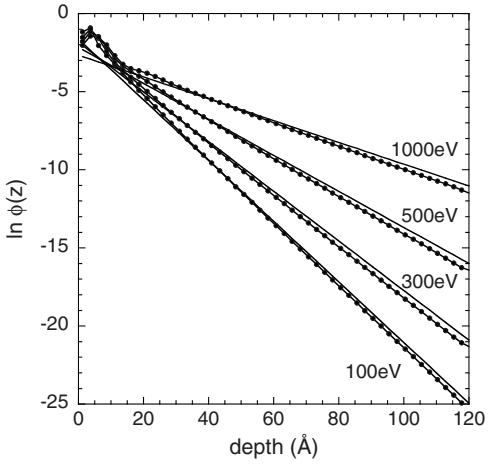

FIG. 10. Depth profile of $\ln \phi(z)$ for different photoelectron energies $\varepsilon_k=100$, 300, 500, and 1000 eV for the chain model used in Fig. 1. Simple exponential DDF $\ln \exp(-z/\lambda)$ with no scatterings from surrounding atoms are also shown by solid lines for comparison.

TABLE I. The bare IMFP λ and the dressed ones λ_d for iron crystals at different ε_k from 100 to 1000 eV. λ_{TPP} is the IMFP of iron calculated by TPP-2M formula (Ref. 42).

ε_k (eV)	λ (Å)	λ_{TPP} (Å)	λ_d (Å)	
			Chain	Cylinder
100	5.15	4.42	5.07	4.98
200	5.15	5.68	5.06	5.02
300	6.29	7.10	6.16	
400	7.49	8.50	7.30	
500	8.67	9.87	8.42	
600	9.85	11.20	9.52	
700	10.99	12.49	10.60	
800	12.12	13.77	11.62	
900	13.23	15.01	12.65	
1000	14.32	16.24	13.64	

materials. The latest version of the IMFP formula proposed by Tanuma *et al.* (TPP-2M) is one of the most frequently used predictive formula to calculate IMFP.[42] In Table I, the IMFP λ_{TPP}, calculated by the TPP-2M formula,[42] is also shown for comparison. We find that $\lambda > \lambda_d$ for all energies considered here. Similar behaviors have also been observed in the Monte Carlo simulation.[10–12]

Figure 11 shows the calculated $\ln \phi(z)$ as function of the depth z for $\varepsilon_k = 100$ and 300 eV. We use the cylinder model

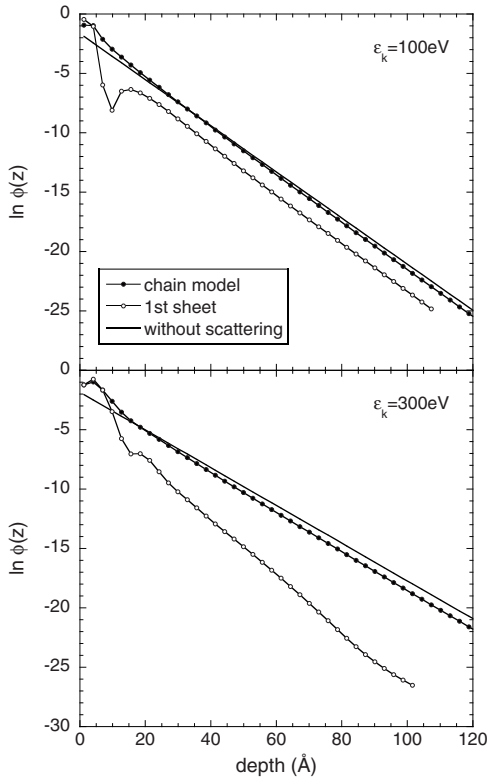

FIG. 11. Same as Fig. 10, but from the cylinder model where only the first nearby sheet is taken into account.

where only the nearby sheet is taken into account (81 layers) because of the computation cost. This model also shows the exponential decay at large z [see Eq. (19)], but λ_d is smaller than that in the chain model; the rapid decay of the DDF in the cylinder model was already observed in Figs. 6 and 7. The DDF shows a dip at ~10 Å for the cylinder model at $\varepsilon_k = 100$ eV, and a small dip at ~15 Å at $\varepsilon_k = 300$ eV. The unexpected dip, however, is lost by use of large cylinder models: The model with up to the third sheet gives no such dip. We, thus, expect that no dip may be observed. As discussed before (see Figs. 6 and 7), the calculated DDF slowly converges with cluster size in the cylinder models. Table I shows that the cylinder model gives different λ_d because of different contributions from elastic scatterings. At 300 eV, $\ln \phi(z)$ is not accurately fitted to a linear function because of the insufficient cluster size used here: A larger cluster should be used to obtain good convergence. The listed λ_d's in Table I for the cylinder model are not so accurate.

IV. CONCLUDING REMARKS

In this work, we study the depth distribution function (DDF) by use of quantum mechanical full multiple scattering calculations. It is necessary to include full multiple scatterings; finite multiple scattering approaches to the DDF calculations are inadequate because finite multiple scatterings diverge with increase of scattering orders.

The full multiple scattering calculations give a prominent peak in the DDF at the second layer from the surface in all the chain models and for all electron energies considered here. This peak is caused by the focusing effects in the forward elastic scatterings, as observed in XPS and EXAFS. The interference can be destroyed by thermal motion of composite atoms, which gives a duller peak with increase of temperature.

Both the chain and the cylinder models give a peak in the DDF $\phi(z)$ from the layer at $z \sim 4.1$ Å, consistent with the observed results[10–13] obtained so far, although there have been no experimental DDF for iron crystal. An important difference in these models is the decaying behavior of $\phi(z)$ at large z: The realistic cylinder models show more rapid decay than the simple chain models. One important result is that $\lambda > \lambda_d$ is also supported by the classical Monte Carlo simulations,[10,11] whereas they are applied to the DDF calculations for amorphous solids.

In the present paper, we only consider the normal emission from the monatomic crystals because of heavy computation cost. In principle, this method can be applied to any complex systems such as Al_2O_3 and CuO crystals, and also the off-normal photoemission. To obtain reliable results for the off-normal emission, we should use large clusters. These studies will be carried out soon.

We clearly show that the IMFP depends on the basic theoretical framework. If we completely neglect elastic scatterings from composite atoms, the conventional bare IMFP λ can be used. On the other hand, if we include the elastic scattering, the IMFP λ is determined on the basis of $\mathrm{Im}\,\Sigma$ in the interstitial region. We also should note that experimental IMFP referring to the decay behavior of the DDF at large z

already includes some contributions from the elastic scatterings.

As demonstrated here, the DDF, in particular, at small z, depends on the details of the surface structure. We, are, thus, afraid that the classical approaches fail to explain the details of the DDF. For that purpose, further experimental efforts are necessary to measure the DDF for different surfaces of single crystals. Further quantum DDF calculations are also to be carried out for other systems and for off-normal emission.

ACKNOWLEDGMENTS

The authors are grateful for financial support from 21 COE program (Frontiers of Super Functionality Organic Device, Chiba University). H.A. is also grateful for the financial support from Fumi Yamamura Memorial Foundation for Female Natural Scientists. The authors would like to acknowledge S. Tanuma for useful discussion and comments on this study.

*shino@graduate.chiba-u.jp

[1] S. Hüfner, *Photoelectron Spectroscopy, Principles and Applications*, 3rd ed. (Springer, New York, 2003).
[2] A. Jablonski, Surf. Sci. **586**, 115 (2005).
[3] O. A. Baschenko and V. I. Nefedov, J. Electron Spectrosc. Relat. Phenom. **17**, 405 (1979).
[4] O. A. Baschenko and V. I. Nefedov, J. Electron Spectrosc. Relat. Phenom. **21**, 153 (1980).
[5] O. A. Baschenko and V. I. Nefedov, J. Electron Spectrosc. Relat. Phenom. **27**, 109 (1982).
[6] W. S. M. Werner, I. S. Tilinin, and M. Hayek, Phys. Rev. B **50**, 4819 (1994).
[7] A. Jablonski and J. Zemek, Surf. Sci. **347**, 207 (1996).
[8] A. Dubus, A. Jablonski, and S. Tougaard, Prog. Surf. Sci. **63**, 135 (2000).
[9] *ASTM Standards on Disc* (ASTM International, Philadelphia, 2006), Vol. 03.06.
[10] I. S. Tilinin, A. Jablonski, J. Zemek, and S. Hucek, J. Electron Spectrosc. Relat. Phenom. **87**, 127 (1997).
[11] S. Hucek, J. Zemek, and A. Jablonski, J. Electron Spectrosc. Relat. Phenom. **85**, 257 (1997).
[12] J. Zemek, P. Jiricek, and K. Olejnik, Surf. Sci. **572**, 93 (2004).
[13] J. Zemek, P. Jiricek, S. Hucek, A. Jablonski, and B. Lesiak, Surf. Sci. **473**, 8 (2001).
[14] W. Bardyszewski and L. Hedin, Phys. Scr. **32**, 439 (1985).
[15] L. Hedin, J. Michiels, and J. Inglesfield, Phys. Rev. B **58**, 15565 (1998).
[16] C. Caroli, D. Lederer-Rozenblatt, B. Roulet, and D. Saint-James, Phys. Rev. B **8**, 4552 (1973).
[17] C.-O. Almbladh, J. Phys.: Conf. Ser. **35**, 127 (2006).
[18] C.-O. Almbladh, Phys. Scr. **32**, 341 (1985).
[19] H. Arai and T. Fujikawa, Phys. Rev. B **72**, 075102 (2005).
[20] T. Fujikawa and H. Arai, J. Electron Spectrosc. Relat. Phenom. **123**, 19 (2002).
[21] T. Fujikawa and H. Arai, Chem. Phys. Lett. **368**, 147 (2003).
[22] T. Fujikawa, J. Phys. Soc. Jpn. **50**, 1321 (1981).
[23] T. Fujikawa, J. Phys. Soc. Jpn. **51**, 251 (1982).
[24] T. Fujikawa, J. Phys. Soc. Jpn. **54**, 2747 (1985).
[25] C. S. Fadley, *Synchrotron Radiation Research, Advances in Surface and Interface Science* (Plenum, New York, 1992), Vol. 1.
[26] P. M. Echenique, J. M. Pitarke, E. V. Chulkov, and A. Rubio, Chem. Phys. **251**, 1 (2000).
[27] T. Fujikawa, K. Nakamura, S. Nagamatsu, and J. J. Rehr, J. Phys. Soc. Jpn. **71**, 357 (2002).
[28] P. H. Dederichs, in *Solid State Physics, Advances in Research and Applications*, edited by F. Seitz, D. Turnbull, and H. Ehrenreich (Academic, New York, 1972), Vol. 27, p. 135.
[29] T. Fujikawa and L. Hedin, Phys. Rev. B **40**, 11507 (1989).
[30] T. Fujikawa, K. Hatada, and L. Hedin, Phys. Rev. B **62**, 5387 (2000).
[31] P. A. Lee and G. Beni, Phys. Rev. B **15**, 2862 (1977).
[32] T. Fujikawa, A. Saito, and L. Hedin, Jpn. J. Appl. Phys., Suppl. **32**, 18 (1993).
[33] G. D. Mahan, *Many-Particle Physics*, 3rd ed. (Kluwer Academic, Dordrecht/Plenum, New York, 2000).
[34] L. Hedin, Phys. Rev. **139**, A796 (1965).
[35] L. Hedin and S. Lundqvist, *Solid State Physics, Advances in Research and Applications*, edited by F. Seitz, D. Turnbull, and H. Ehrenreich (Academic, New York, 1969), Vol. 23, p. 1.
[36] T. Fujikawa and T. Miyanaga, J. Phys. Soc. Jpn. **62**, 4108 (1993).
[37] P. Rennert, J. Phys. IV **7**, 147 (1997).
[38] T. Fujikawa, J. J. Rehr, Y. Wada, and S. Nagamatsu, J. Phys. Soc. Jpn. **68**, 1259 (1999).
[39] T. Miyanaga and T. Fujikawa, J. Phys. Soc. Jpn. **63**, 1036 (1994).
[40] Y. Chen, F. J. García de Abajo, A. Chassé, R. X. Ynzunza, A. P. Kaduwela, M. A. Van Hove, and C. S. Fadley, Phys. Rev. B **58**, 13121 (1998).
[41] J. J. Rehr and R. C. Albers, Rev. Mod. Phys. **72**, 621 (2000).
[42] S. Tanuma, C. J. Powell, and D. R. Penn, Surf. Interface Anal. **17**, 911 (1991).